Article | Open Access

Energy Materials

Jin *et al. Energy Mater.* **2026**, *6*, 600149 **DOI:**10.20517/energymater.2026.271

Metal-dependent Volmer free energies track opposite cation trends on Pt(111) and Au(111) as catalysts for hydrogen evolution

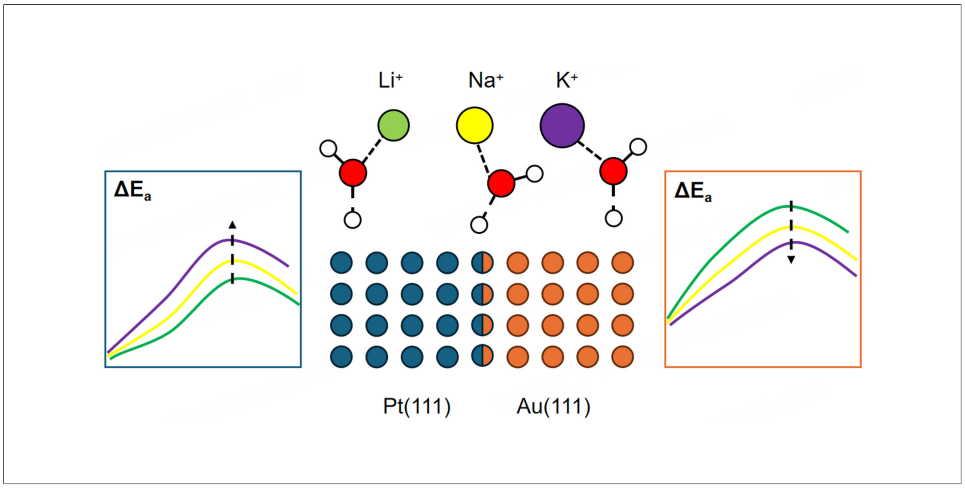
Fangrun Jin[1,#], Meng Cao[1,#], Hao Tian[1,2,*], Xinyu Wang[3,4], Wei Zhang[3,4], Xiangqiong Shen[3,4], Chuanhui Zhu[1,5,*], S. Y. Tong[1,5,6,*]

Keywords:
Alkaline hydrogen evolution reaction, alkali-metal cations, Volmer step, constrained ab initio molecular dynamics, electric double layer, Pt/Au interfaces

Citation: Jin, F.; Cao, M.; Tian, H.; Wang, X.; Zhang, W.; Shen, X.; Zhu, C.; Tong, S. Y. Metal-dependent Volmer free energies track opposite cation trends on Pt(111) and Au(111) as catalysts for hydrogen evolution. *Energy Mater.* **2026**, *6*, 600149. https://dx.doi.org/10.20517/energymater.2026.271

Received: 14 Aug 2026 **First Decision:** 28 Aug 2026 **Revised:** 26 Sep 2026 **Accepted:** 16 Oct 2026 **Published:** 29 Oct 2026

Academic Editor: Ho Won Jang
Copy Editor: Fangling Lan
Production Editor: Fangling Lan



Abstract

The hydrogen evolution reaction in alkaline media exhibits opposite alkali-cation activity trends on Pt and Au, but the microscopic origin of this inversion remains unresolved. In this work, we combine electrochemical measurements and *in situ* Raman spectroscopy on polycrystalline Pt and Au with constrained ab initio molecular dynamics (AIMD) simulations of Pt(111)/water and Au(111)/water interfaces. The results show the following. (i) Larger alkali-metal cations increase the fitted high-wavenumber Raman contribution associated with weakly hydrogen-bonded water on both Pt and Au, with a more pronounced effect on Pt. In the simulations, increasing interfacial cation number broadens the local water-depleted region. (ii) Cation positioning follows a monotonic size ordering on Pt(111), where larger cations reside closer to the surface, whereas on Au(111) the cation-height sequence is nonmonotonic. (iii) Most importantly, single-cation constrained AIMD free-energy profiles for the Volmer step recover the qualitative inversion observed on polycrystalline Pt and Au. This agreement suggests that the Volmer barrier in the model

[1]School of Science and Engineering, The Chinese University of Hong Kong, Shenzhen 518172, Guangdong, China.
[2]Institute of Nanotechnology and Intelligence (inAI), Jinan University, Guangzhou 511443, Guangdong, China.
[3]Inner Mongolia Huadian Huayang Hydrogen Energy Technology Co., Ltd., Baotou 014500, Inner Mongolia, China.
[4]Huadian Inner Mongolia Energy Co., Ltd., Hohhot 010020, Inner Mongolia, China.
[5]Institute of Renewable Energy on Demand, School of Materials Science and Engineering, Suzhou University of Science and Technology, Suzhou 215009, Jiangsu, China.
[6]Department of Physics, Southern University of Science and Technology, Shenzhen 518055, Guangdong, China.
[#]Authors contributed equally.

***Correspondence to:** Prof. Hao Tian, School of Science and Engineering, The Chinese University of Hong Kong, Shenzhen 518172,

Guangdong, China; Institute of Nanotechnology and Intelligence (inAI), Jinan University, Guangzhou 511443, Guangdong, China. E-mail: tianhao@cuhk.edu.cn; Prof. Chuanhui Zhu, School of Science and Engineering, The Chinese University of Hong Kong, Shenzhen 518172, Guangdong, China; Institute of Renewable Energy on Demand, School of Materials Science and Engineering, Suzhou University of Science and Technology, Suzhou 215009, Jiangsu, China. E-mail: zhuchh6@mail2.sysu.edu.cn; Prof. S. Y. Tong, School of Science and Engineering, The Chinese University of Hong Kong, Shenzhen 518172, Guangdong, China; Institute of Renewable Energy on Demand, School of Materials Science and Engineering, Suzhou University of Science and Technology, Suzhou 215009, Jiangsu, China. E-mail: tongsy@cuhk.edu.cn

may be an intrinsic contributing factor to the observed experimental trends.

INTRODUCTION

Alkaline hydrogen electrocatalysis remains kinetically limited, with Volmer kinetics depending on both water dissociation and the structure of the catalyst-electrolyte interface[1]. On Pt, the benchmark catalyst for the hydrogen evolution reaction/hydrogen oxidation reaction (HER/HOR), rates in alkaline media are commonly orders of magnitude lower than those in acidic media[2,3]. The conventional hydrogen-binding-energy descriptor provides an established framework for acidic HER[4], but does not fully account for this kinetic penalty because water dissociation, hydroxide-related species, and interfacial solvent reorganization also become important in alkaline media[5-9]. Recent studies further resolve interfacial water orientation and hydroxide solvation as distinct contributions to alkaline hydrogen electrocatalysis[10-12]. For the reverse HOR on Pt, pH-dependent coupling between water reorientation and adsorbed hydrogen has also been identified[13]. The electrolyte therefore acts as more than an ionic conductor, as cations interact with surface species and modify the electric double layer[14-16]. Their influence on interfacial water organization and elementary reaction energetics makes cation identity an important variable in understanding alkaline HER.

The importance of cation identity is particularly evident in the contrasting HER trends reported for different metals. Activity has been reported to decrease with increasing cation size on reactive metals such as Pt and Ir, but to increase on more inert metals such as Au and Ag[17]. These trends also depend on cation concentration, pH, overpotential, and catalyst structure[18,19]. Impedance measurements also indicate cation-dependent contributions of the Volmer-Heyrovsky and Volmer-Tafel pathways on Pt[20]. Electrostatic descriptions relate this behavior to cation positions in the double layer and the local fields experienced by reaction intermediates and transition states[21,22]. A mean-field treatment explicitly separates water reduction from hydroxide transfer through the double layer[23]. At the level of elementary reaction steps, cation stabilization of the water-dissociation transition state and hydroxide product has been proposed to facilitate Volmer activation on Au while hindering hydroxide removal on Pt[24]. Cation accumulation can also inhibit HER by restricting access to surface sites[18]. Its effects extend into the surrounding water network, where reduced hydrogen-bond connectivity can impede proton transfer through the double layer[25-27]. Recent interfacial spectroscopy has additionally linked cation hydration to water orientation on Pt and identified K^+-associated proton shuttling during HER on Au[28,29]. Chen *et al.* further showed that cations can facilitate Volmer water dissociation on Pt(100), while larger cations disrupt interfacial hydrogen bonding and hinder hydroxide migration[30]. Together, these studies indicate that cations can affect local reaction energetics and interfacial transport in different ways, making their respective contributions difficult to separate from overall activity alone.

It therefore remains unclear whether the experimentally observed Pt/Au cation-trend inversion can arise from the intrinsic Volmer barrier under defined single-cation conditions. Comparing Volmer free-energy profiles on Pt(111) and Au(111) provides a way to assess this local energetic contribution without explicitly representing dense cation accumulation or long-range transport. Explicit water-metal interface simulations offer a suitable framework by resolving solvent organization and reaction free energies beyond static

adsorption energetics[31-33]. In this study, electrochemical measurements and *in situ* Raman spectroscopy on polycrystalline Pt and Au are combined with constrained ab initio molecular dynamics (AIMD) simulations of Li^+, Na^+, and K^+ at Pt(111)/water and Au(111)/water interfaces. Raman spectroscopy characterizes the cation-dependent interfacial-water response, while AIMD resolves local cation distributions and water organization at the model interfaces. The calculated Volmer free-energy profiles reproduce the qualitative Pt/Au cation-trend inversion under single-cation conditions. This result shows that the metal-dependent Volmer response can generate opposite cation orderings within the model and may contribute intrinsically to the experimental trends.

EXPERIMENTAL

Electrochemical measurements

Electrochemical measurements were performed at room temperature using a CHI760E electrochemical workstation (Chenhua) in a standard three-electrode configuration. A mercury/mercury oxide (Hg/HgO) electrode and a Pt wire were used as the reference and counter electrodes, respectively. All potentials reported in this work were converted to the reversible hydrogen electrode (RHE) scale. Polycrystalline Pt and Au were used as the working electrodes.

Before the HER and spectroscopic measurements, the working electrodes were preconditioned by cycling twice between 0.02 and 1.20 V *vs*. RHE at 100 mV s^{-1} in Ar-saturated 0.1 M LiOH, NaOH, or KOH (pH = 13 ± 0.1). HER polarization curves were recorded at 5 mV s^{-1} without real-time iR compensation. The uncompensated resistance, R_u, was determined under the corresponding measurement conditions. The measured R_u values are provided in the Supplementary Materials. The original linear sweep voltammetry curves were corrected after measurement according to $E_{corrected} = E_{measured} - iR_u$, where i is the signed measured current in amperes and R_u is the uncompensated resistance in ohms. The full measured R_u value was used for the correction. Freshly prepared electrolytes were used for all measurements.

In situ Raman spectra were collected at -0.05 V *vs*. RHE in the same electrolyte series to compare interfacial water at a fixed applied potential. The O-H stretching envelope was fitted with three overlapping components. Literature assignments associate the lower- and intermediate-wavenumber components with four- and two-coordinated hydrogen-bonded water, respectively, and the high-wavenumber component with weakly hydrogen-bonded cation-hydrated water[34,35]. These assignments are used phenomenologically for the present Pt and Au spectra. The same peak-position settings were used across all spectra. Each component area was normalized by the sum of the three integrated areas. These fractions represent relative spectral contributions rather than molecular population fractions. Because the weak high-wavenumber component can be sensitive to fitting constraints, its area fraction is used only for semiquantitative comparison. Further definitions are provided in the Supplementary Materials.

Computational methods

Structure optimizations and AIMD simulations were performed using the Vienna ab initio simulation package[36]. Electron-ion interactions were described using the projector augmented-wave method[37], and exchange-correlation effects were treated with the Perdew-Burke-Ernzerhof functional within the generalized gradient approximation[38]. Grimme's D3 dispersion correction was included to account for van der Waals interactions[39]. The plane-wave kinetic-energy cutoff was 500 eV. Geometry optimizations were converged to a maximum force of 0.02 eV $Å^{-1}$ and a total-energy change of 10^{-6} eV. Brillouin-zone sampling was restricted to the Γ point, symmetry was disabled, and first-order Methfessel-Paxton smearing with a width of 0.2 eV was used for the metallic slabs[40]. All simulation cells were charge neutral, with no electrons added to or removed from the neutral stoichiometric electron count. The comparison concerns qualitative cation ordering, not matched electrode potentials or electrolyte concentrations.

Explicit Pt(111)/water and Au(111)/water interface models were constructed following established simulation strategies for hydrogen electrocatalysis[31-33]. Each model contained a four-layer orthogonal metal slab in contact with 60 explicit water molecules. A vacuum region was included, giving a total cell length of approximately 4.9 nm along the z direction. The lateral cell dimensions were 11.09 × 9.60 Å^2 for Pt(111) and 11.57 × 10.02 Å^2 for Au(111). To define the modeled surface states, the adsorbed-hydrogen (H_{ad}) coverages were set to 0.63 monolayer (ML, defined per surface metal atom) for Pt(111)[41] and 0.00 ML for Au(111)[42,43]. Unless otherwise specified, one alkali-metal cation (Li^+, Na^+, or K^+) was introduced into the interfacial water region of each periodic cell to define the single-cation condition used for the Volmer free-energy calculations. Additional Pt(111)/water models containing two or three K^+ ions were constructed to examine how cation accumulation affects the water distribution.

Unconstrained AIMD simulations were first performed for 20-30 ps with a 1 fs time step in the canonical ensemble at constant particle number, volume, and temperature at 298 K using a Nosé-Hoover thermostat[44,45]. Equilibrated configurations were then used to initialize constrained AIMD simulations of the Volmer water-dissociation step. Free-energy profiles were obtained with a slow-growth constrained-dynamics protocol[46], using the collective variable (CV) defined as CV = d(O-H) - d(M-H), where d(O-H) is the breaking O-H bond length of an H-down interfacial water molecule and d(M-H) is the distance between the transferring H atom and the target surface metal atom. The CV was advanced by 0.0003 Å per 1 fs step for 10,000 steps, corresponding to a nominal pulling rate of 0.3 Å ps^{-1} over 10 ps. This small increment was chosen to reduce numerical uncertainty associated with finite increments along the slow-growth path by limiting the change in the constraint at each update. Free-energy differences were obtained by integrating the mean constraint force along the CV. Further computational details are provided in the Supplementary Materials. Structural statistics were calculated from the final 5 ps of each full unconstrained trajectory, after the preceding interfacial relaxation. Water-profile normalization, the operational definition of the nearest water layer, and numerical Volmer barriers are provided in Supplementary Text and Supplementary Table 1.

RESULTS AND DISCUSSION

Opposite HER activity trends despite shared interfacial-water responses

Figure 1 compares HER polarization, fixed-current overpotentials, and Raman spectra for polycrystalline Pt in panels (A-C) and Au in panels (D-F), measured in 0.1 M LiOH, NaOH, and KOH. The electrochemical measurements show opposite cation-dependent activity trends. At a cathodic current density of -5 mA cm^{-2}, the overpotential magnitude on Pt increases from 0.189 V in LiOH to 0.224 V in NaOH and 0.248 V in KOH [Figure 1A and B], giving the activity order $Li^+ > Na^+ > K^+$. On Au, the corresponding values decrease from 0.532 to 0.517 and 0.499 V, giving the reverse activity order [Figure 1D and E]. Pt remains more active in every electrolyte, while the direction of the cation effect depends on the metal. This distinction between the activity of each metal and its response to cation identity agrees with earlier Pt/Au comparisons and studies of catalyst-structure-dependent cation effects[17-19].

The experimental cation ordering provides the benchmark for the Pt(111)/water and Au(111)/water simulations. Experimental and calculated reference X-ray diffraction patterns are shown in Supplementary Figure 1. The close-packed (111) facets provide well-defined models with relatively low clean-surface energies among the low-index facets of both metals[47,48]. These interfaces allow cation identity to be varied systematically within each metal series, enabling comparison of the elementary Volmer response with the direction of the polycrystalline activity trends. The comparison therefore concerns the cation ordering rather than a quantitative correspondence between a polycrystalline electrode and a single modeled facet. Constant-potential simulations of stepped Pt further show that cation-facet coupling can modify water activation[49], highlighting the complementary roles of terrace and stepped sites in interpreting polycrystalline activity.

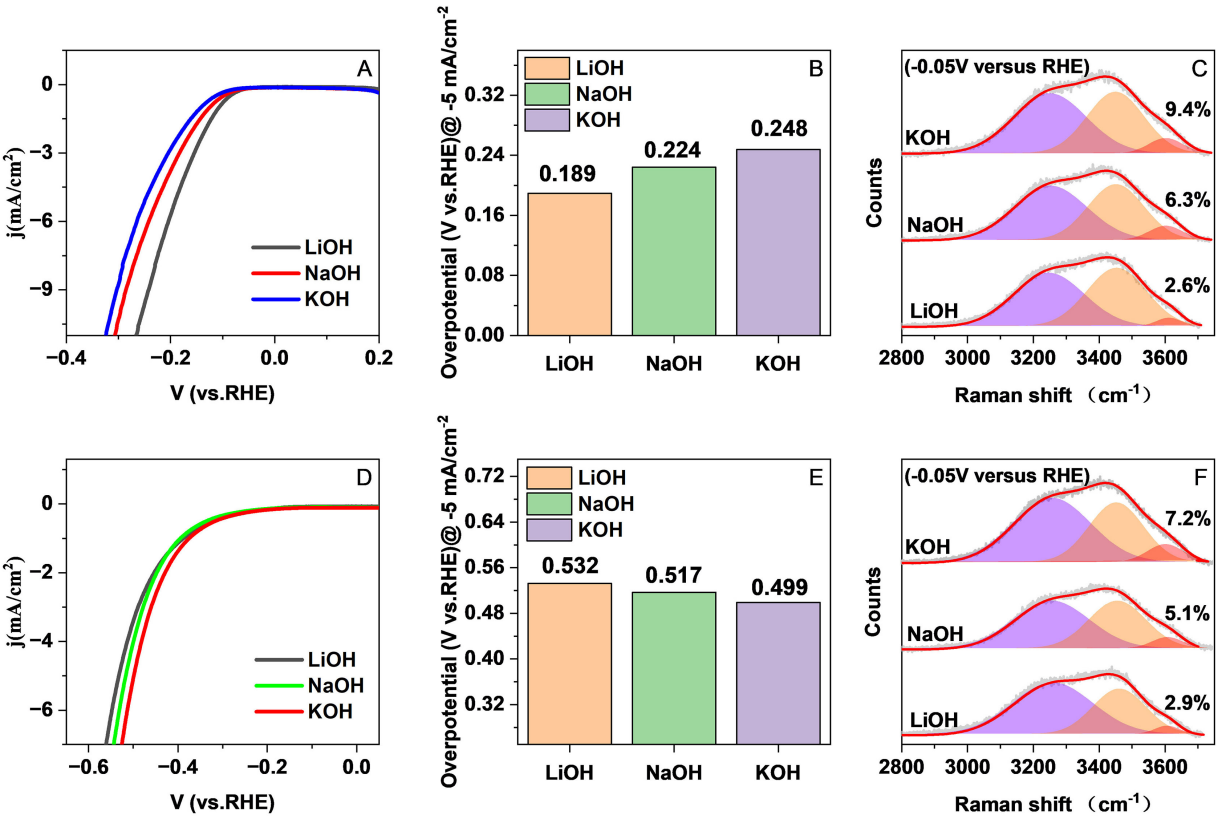


Figure 1. Cation-dependent HER activity and Raman spectra on polycrystalline Pt and Au. Panels (A-C) show Pt and panels (D-F) show Au in 0.1 M LiOH, NaOH, and KOH. (A and D) Polarization curves after post-measurement iR correction. (B and E) Overpotential magnitudes at a cathodic current density of -5 mA cm^{-2}. (C and F) Raman O-H stretching spectra at -0.05 V vs RHE and their three-component fits. The lower- and intermediate-wavenumber components are assigned phenomenologically to four- and two-coordinated hydrogen-bonded water, respectively. The high-wavenumber component is associated with weakly hydrogen-bonded cation-hydrated water. The numerical labels in (C and F) are the integrated area percentages of the high-wavenumber component: 100% × $A_{weak}/(A_{strong} + A_{moderate} + A_{weak})$. In LiOH, NaOH, and KOH order, these values are 2.6%, 6.3%, and 9.4% for Pt and 2.9%, 5.1%, and 7.2% for Au. They quantify fitted spectral contributions, not molecular population fractions.

In situ Raman spectra at -0.05 V *vs.* RHE reveal a similar interfacial-water response on the two metals [Figure 1C and F]. The high-wavenumber component near 3,600 cm^{-1} is associated with weakly hydrogen-bonded cation-hydrated water, following assignments in Raman studies of Pd interfaces[34,35]. Its fitted contribution increases from Li^+ to K^+ on both Pt and Au, with a more pronounced change on Pt. This increase indicates a larger spectral contribution from weakly hydrogen-bonded environments in the presence of larger cations. The calculated vibrational density of states likewise shows an increased high-frequency O-H stretching contribution on Pt(111) and Au(111) [Supplementary Figure 2]. These spectral responses are consistent with cation-dependent interfacial-water reorganization, which has been implicated in double-layer proton transfer[25-27,50].

Importantly, the Raman response changes in the same direction on both electrodes, whereas the HER activity trend reverses between the metals. Increasing cation size enhances the weakly hydrogen-bonded O-H stretching contribution but lowers HER activity on polycrystalline Pt and raises it on polycrystalline Au. The fixed-potential spectra provide a structural reference for examining these contrasting responses, rather than a direct measure of water structure at the different potentials used for the activity comparison. The AIMD analysis first resolves cation hydration and the spatial distribution of water at Pt(111) and Au(111), then

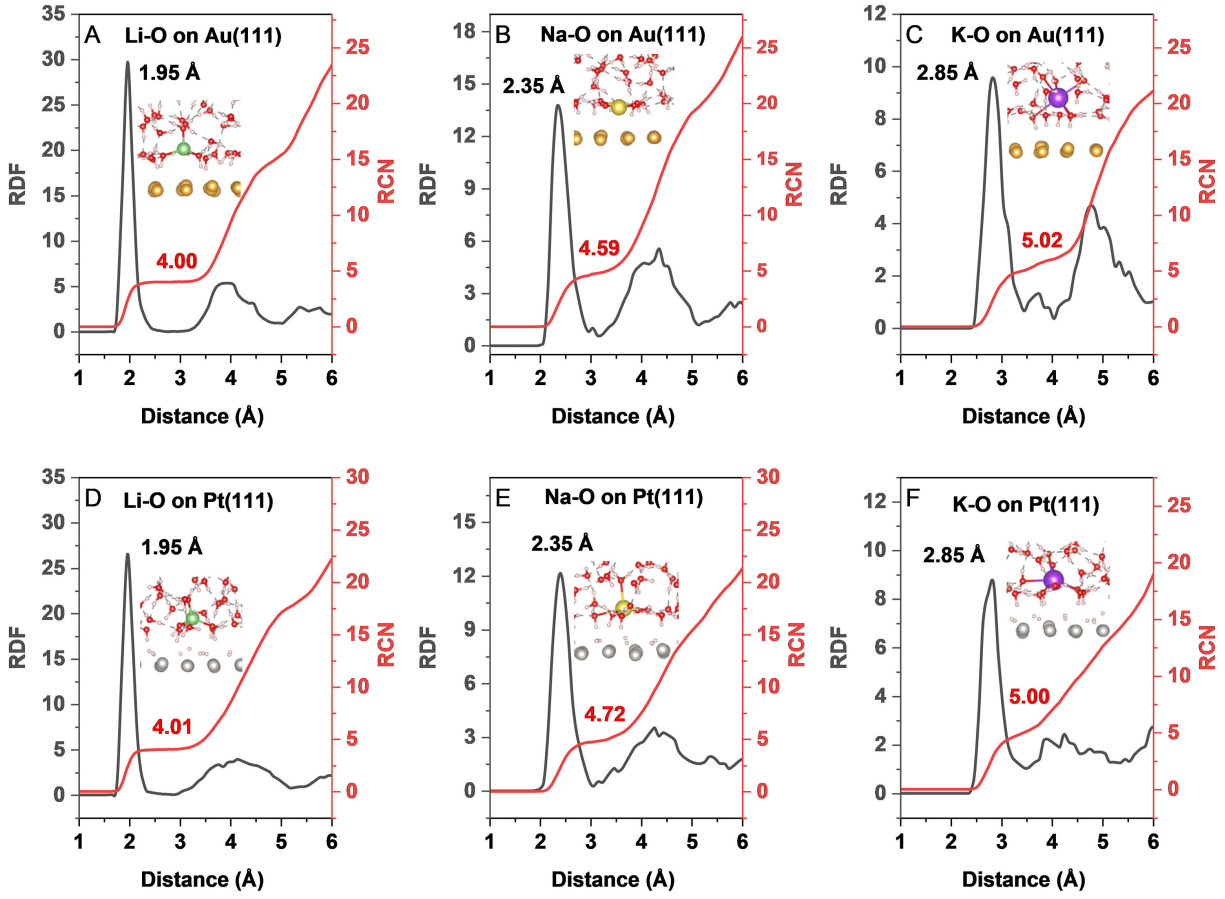


Figure 2. Interfacial cation hydration from AIMD. Cation-O(water) radial distribution functions (RDFs, gray, left axis) and running coordination numbers (RCNs, red, right axis) for Li^+, Na^+, and K^+ at Au(111) in (A-C) and Pt(111) in (D-F). Within each group, the panels follow the order Li^+, Na^+, and K^+. Black annotations identify the first RDF maxima in Å, and red annotations give the first-shell coordination numbers. Statistics were calculated from the final 5 ps of the unconstrained trajectories. Insets show representative hydration configurations rendered using VESTA 3.5.8.[53].

evaluates the single-cation Volmer free energies and the geometry of the reacting water. In concentrated lithium bis(trifluoromethanesulfonyl)imide at Au(111), cation accumulation and electric-field changes can also alter water orientation and vibrational signatures[51]. That concentrated-electrolyte regime is distinct from the dilute hydroxide solutions examined here.

Cation hydration and spatial redistribution of interfacial water

Unconstrained AIMD characterizes the cation hydration shell and its arrangement relative to the metal surface[31-33,52]. The cation-O radial distribution functions in Figure 2 have first-shell maxima at approximately 1.95, 2.35, and 2.85 Å for Li^+, Na^+, and K^+, respectively, on Pt(111) and Au(111). The corresponding first-shell coordination numbers increase from about four for Li^+ to 4.6-4.7 for Na^+ and about five for K^+. The sharp Li-O peak indicates a narrowly defined first hydration shell, whereas the broader K-O peak reflects a wider distribution of cation-water separations. For a given cation, the first-shell distances and coordination numbers are similar on Pt(111) and Au(111). Thus, the local hydration shell primarily reflects cation identity, while metal-dependent differences emerge in the positions of the hydrated cations and surrounding water. Atomic configurations were visualized using VESTA 3.5.8.[53].

The water-number profiles reveal how the cations redistribute interfacial water [Figure 3A and B]. The ordinate is the trajectory-averaged number of water molecules per 0.02 Å surface-normal bin. For the Pt(111) and Au(111) bin volumes, the bulk-water reference of 0.056 mol cm^{-3} gives approximately 0.07 and 0.08

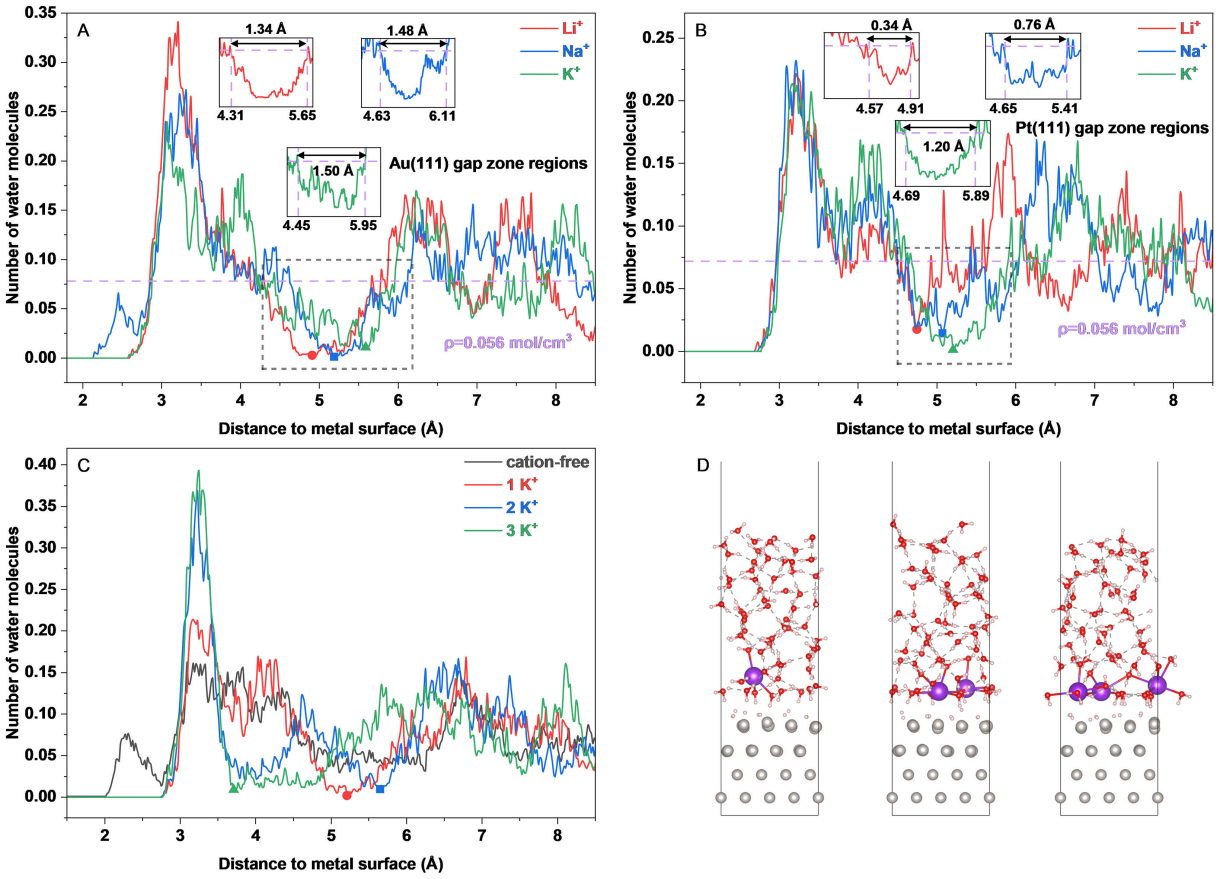


Figure 3. Interfacial water counts per spatial bin and representative configurations from AIMD. (A and B) Profiles for Li^+, Na^+, and K^+ at (A) Au(111)/water and (B) Pt(111)/water interfaces, averaged over the final 5 ps of the unconstrained trajectories. Insets show the two reference-level crossings that delimit each local water-depleted region and its width in Å. The ordinate is the time-averaged number of water molecules per bin. Bins have a thickness of 0.02 Å and volumes of 2.32 $Å^3$ for Au(111) and 2.13 $Å^3$ for Pt(111). The purple line is the count equivalent of the bulk-water density, 0.056 mol cm^{-3}: 0.08 molecules per bin in (A) and 0.07 in (B). Normalization and unit conversion are specified in Supplementary Text. (C) Profiles for Pt(111) without cations and with one, two, or three interfacial K^+ ions. (D) Representative Pt(111)/water configurations containing one, two, and three K^+ ions from left to right, rendered using VESTA 3.5.8.[53].

molecules per bin, respectively. The water-depletion width is the separation between the two crossings of the reference level annotated as bulk-water density, following the construction used by Li *et al.*[25]. The widths increase from 0.34 to 0.76 and 1.20 Å on Pt(111), compared with 1.34, 1.48, and 1.50 Å on Au(111), in the order Li^+, Na^+, and K^+. The Li^+-to-K^+ increase is therefore 0.86 Å on Pt(111) but only 0.16 Å on Au(111). On Pt(111), the solution-side boundary moves from 4.91 to 5.89 Å, whereas the metal-side boundary changes only from 4.57 to 4.69 Å. Larger cations therefore extend the depleted region mainly toward the solution, increasing the separation between near-surface water and the surrounding solvent. This separation may affect the hydration of the hydroxide formed during Volmer activation and provides a structural basis for examining solvent reorganization alongside the reaction barrier, especially on Pt(111).

Increasing the number of interfacial K^+ ions on Pt(111) strengthens the near-surface water peak around 3.2 Å while broadening the adjacent depleted region [Figure 3C and D]. Cation accumulation therefore enriches the nearest layer while increasing its separation from the outer solvent, with possible consequences for hydroxide hydration and hydrogen-bond-mediated proton transfer[25-27,50]. Related AIMD work on Cr-Ir oxides associated greater interfacial hydrogen-bond connectivity with facilitated water dissociation and proton transfer in acidic oxygen evolution[54]. Here, the multi-K^+ models probe water structure, whereas the Volmer profiles below use one cation per periodic cell. This defines a particular interfacial state rather than a

concentration-matched model of 0.1 M electrolyte. At higher coverage, additional cation coordination could stabilize the developing hydroxide, while water redistribution could alter the solvent-reorganization cost. The net effect on the activation free energy depends on the relative stabilization of the reactant and transition region. The structural profiles alone therefore cannot determine whether the single-cation model overestimates or underestimates the barrier response, or whether its cation ordering persists at higher coverage. Assessing these effects requires multi-cation free-energy comparisons, which introduce additional complexity to the mechanistic analysis and fall beyond the scope of the present study.

Water orientation adds the geometry of the O-H bonds to this spatial description. Representative reorientation and water-dipole profiles are shown in Supplementary Figures 3 and 4. On Au(111), cation addition suppresses the narrow positive O-down contribution closest to the surface and deepens the neighboring negative H-down contribution near 3.2 Å [Supplementary Figure 4A]. The cation-free profile already contains a negative first-layer contribution, so this change is not a complete reversal from O-down to H-down water. An H-down geometry directs hydrogen toward the metal and can accommodate a more outward oxygen position, as illustrated by the representative reorientation in Supplementary Figure 3. Because the profiles sum cos(α) within each spatial bin, they reflect both local water occupancy and orientation. They therefore describe the orientational environment available for H transfer during Volmer activation. Hydration, water distribution, and orientation together define the local reaction environment, whose energetic consequences are assessed by the free-energy profiles below.

Single-cation Volmer barriers recover the opposite activity trends

Constrained AIMD evaluates the free energy of Volmer water dissociation in an explicit interfacial solvent[31-33,46,52]. An H-down water molecule with the smallest H-to-surface distance was selected as the reactant. The collective variable, CV = d(O-H) - d(M-H), follows O-H bond cleavage as hydrogen approaches the target surface metal atom to form adsorbed hydrogen, H_{ad}, and interfacial hydroxide. Figure 4A and B shows the free-energy profiles near the barrier. The full profiles and reacting-oxygen distances are provided in Supplementary Figure 5, and representative dissociation snapshots are shown for Pt(111) and Au(111) in Supplementary Figures 6 and 7, respectively. Supplementary Table 1 lists all eight reported barrier estimates, extracted as the profile maxima preceding adsorption of the transferring hydrogen. The cation-free values are 1.49 eV for Pt(111) and 1.83 eV for Au(111). For the cation-free model states, the Pt(111) barrier is approximately 0.34 eV lower than the Au(111) barrier, consistent with the higher measured activity of polycrystalline Pt. The cation-containing profiles reveal how each interfacial environment modifies this elementary activation process within its metal series.

The central energetic result is that the single-cation Volmer barriers reproduce the opposite experimental activity trends qualitatively. On Pt(111), the reported barrier increases from 1.54 to 1.65 and 1.70 eV in the order Li^+, Na^+, and K^+ [Figure 4B and Supplementary Table 1], matching the progressively larger overpotential required from LiOH to KOH. On Au(111), the reported barrier decreases from 1.79 to 1.75 and 1.64 eV over the same cation series [Figure 4A and Supplementary Table 1], matching the increasing activity. The cation-free profiles further clarify the metal dependence. All three cations lower the Au(111) barrier, whereas the profiles of all three cations on Pt(111) lie above the cation-free profile. Thus, cation identity changes the energetic cost of the local Volmer process in opposite directions on the two model surfaces. By contrast, the water-depleted region broadens on both Pt(111) and Au(111) [Figure 3A and B], so its width alone does not predict the direction of the barrier change. The agreement between barrier ordering and activity ordering suggests that the Volmer barrier in the single-cation models may contribute intrinsically to the experimental inversion. Without independent repeats or pulling-convergence tests, the 0.04 eV Li^+/Na^+ difference on Au(111) is interpreted as a qualitative ordering, not a statistically resolved separation.

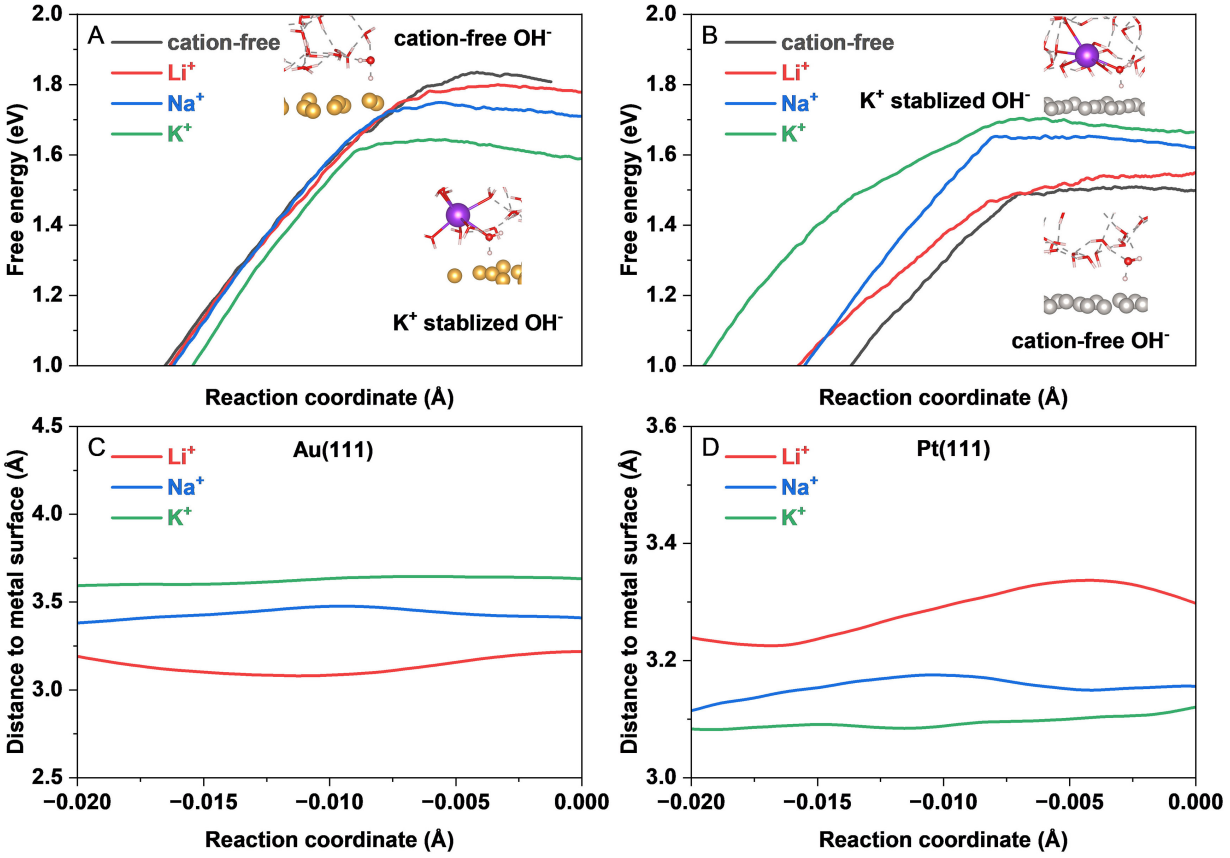


Figure 4. Constrained AIMD profiles for Volmer water dissociation. (A and B) Free-energy profiles near the barrier on (A) Au(111) and (B) Pt(111) without cations and with one Li^+, Na^+, or K^+ ion. (C and D) Surface-normal distance of the reacting oxygen from (C) Au(111) and (D) Pt(111) over the displayed CV window. The CV is d(O-H) - d(M-H), with M denoting the target surface metal atom. Gray, red, blue, and green curves denote cation-free, Li^+, Na^+, and K^+ conditions, respectively. Insets in (A and B) show local hydroxide environments under cation-free conditions (upper inset in (A); lower inset in (B)) and with K^+ (lower inset in (A); upper inset in (B)), rendered using VESTA 3.5.8.[53]. Full profiles are given in Supplementary Figure 5. Supplementary Table 1 lists all eight barrier estimates. Trajectory snapshots are provided for Pt(111) and Au(111) in Supplementary Figures 6 and 7, respectively.

Despite the opposite cation orderings, both model surfaces exhibit the same relationship between reacting-oxygen distance and Volmer barrier. Across the CV window in Figure 4C and D, the reacting oxygen lies progressively farther from Au(111) in the order $Li^+ < Na^+ < K^+$, while its distance from Pt(111) follows $Li^+ > Na^+ > K^+$. Within each metal series, the lower-barrier profiles have greater reacting-oxygen distances throughout the displayed window. The Pt(111) and Au(111) snapshots in Supplementary Figures 6 and 7 illustrate the corresponding dissociation configurations. The mechanistic analysis below examines how cation positioning and water organization could favor opposite reacting-oxygen orderings at these two interfaces.

Metal-dependent coupling between cation position and reacting-water geometry

The unconstrained trajectories show distinct cation-positioning patterns at the two interfaces [Figure 5A and B]. Over the final 5 ps, the mean cation-surface distance on Pt(111) decreases from Li^+ to Na^+ to K^+. On Au(111), Li^+ also remains farthest from the surface on average, while the Na^+ and K^+ trajectories overlap and Na^+ has the smaller mean distance. The monotonic size ordering on Pt(111), compared with the Na^+/K^+ reversal on Au(111), suggests that the balance between cation hydration and approach to the surface depends on the metal. Cation identity and interfacial position both influence double-layer structure[16,21,55], and the weaker hydration of larger alkali ions offers a rationale for their closer approach in the present

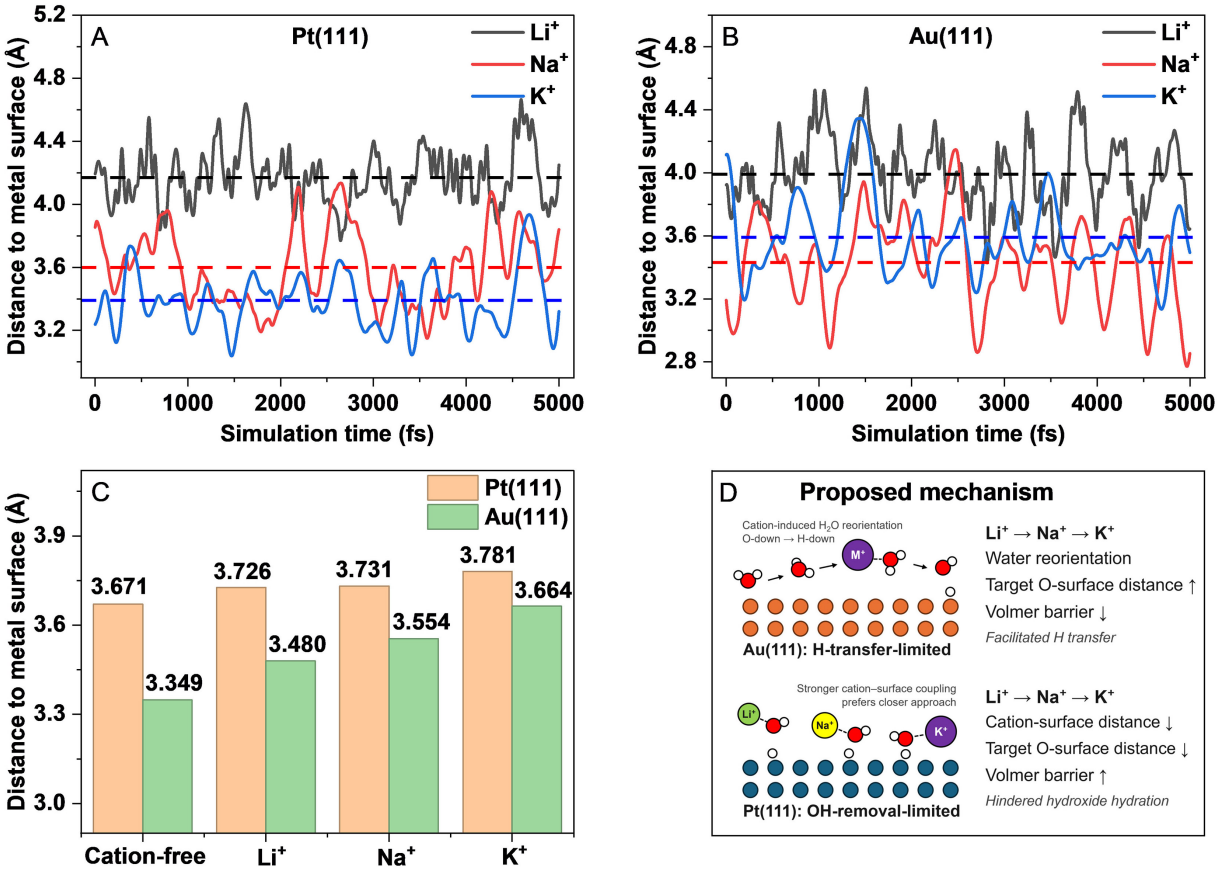


Figure 5. Cation positioning, nearest-water-layer distances, and a proposed mechanism for the metal-dependent Volmer response. (A and B) Cation-surface distances on (A) Pt(111) and (B) Au(111) during the final 5 ps of the unconstrained trajectories. Dashed lines indicate mean cation-surface distances over the 5 ps intervals. Gray, red, and blue denote Li^+, Na^+, and K^+, respectively. (C) Mean nearest-water-layer distances on Pt(111) in orange and Au(111) in green for cation-free and single-cation models, calculated over the same interval. The reference plane is the instantaneous mean z coordinate of the topmost metal atoms. Water oxygen atoms within 5.00 Å above this plane are selected irrespective of orientation; the reported values are averages of the per-frame mean oxygen-surface distances, not density-peak positions. (D) Proposed H-transfer-limited character on Au(111) in the upper schematic and OH-removal-limited character on Pt(111) in the lower schematic. Target O denotes the reacting oxygen, and M^+ denotes a generic monovalent cation. Orange, blue-green, red, and white spheres represent Au, Pt, O, and H. On Pt(111), Li^+, Na^+, and K^+ are green, yellow, and purple, respectively.

Pt(111) models[56]. Recent combined impedance and AIMD analysis of alkaline Pt interfaces also links double-layer capacitance to interfacial-water polarization and its potential dependence[57].

The nearest-water-layer distances quantify a different aspect of the solvent response [Figure 5C]. Here, the nearest layer is operationally defined as water oxygen atoms within 5.00 Å above the instantaneous mean z coordinate of the topmost metal layer, including both O-down and H-down configurations. The oxygen-surface distances are first averaged within each frame and then averaged over the final 5 ps. This quantity is a mean position of the selected water layer, not the position of a water-density maximum. The mean distance on Pt(111) increases from 3.671 Å without cations to 3.726, 3.731, and 3.781 Å with Li^+, Na^+, and K^+, respectively. The corresponding Au(111) values are 3.349, 3.480, 3.554, and 3.664 Å. From Li^+ to K^+, the nearest layer therefore moves outward by 0.055 Å on Pt(111) but by 0.184 Å on Au(111). Notably, Au(111) exhibits the larger layer shift, whereas Pt(111) exhibits the larger increase in water-depletion width [Figure 3A and B]. On Au(111), cation addition also suppresses the near-surface positive O-down contribution and deepens the adjacent negative H-down contribution in Supplementary Figure 4A. The cation-free Pt(111) profile already has a more negative first-layer contribution [Supplementary Figure 4B]. These comparisons suggest examining solvent separation on Pt(111) and near-surface water geometry on Au(111) as distinct aspects of their Volmer reaction environments.

Figure 5D summarizes a proposed mechanism for these contrasting responses. On Pt(111), both the cations and the reacting oxygen lie closer to the surface from Li^+ to K^+ [Figures 5A and 4D]. Cation-oxygen coordination may favor this surface-proximal geometry as hydroxide character develops in the reacting water. Meanwhile, the nearest water layer shifts outward and the water-depleted region extends toward the solution, increasing the separation between the reacting oxygen and the surrounding solvent. This arrangement could require greater solvent reorganization to hydrate the developing hydroxide during activation, even if a nearby cation stabilizes the oxygen-containing species electrostatically. The proposed OH-removal-limited character on Pt(111) refers to this local solvent-side accommodation of the emerging hydroxide within the Volmer step. It provides a possible explanation for the higher barriers with larger cations through their effects on the reacting-water geometry and hydration environment.

On Au(111), Na^+ is closer to the surface on average than K^+, yet K^+ yields the lower Volmer barrier [Figures 5B and 4A]. The cation-height sequence therefore points to a role for water orientation beyond surface approach alone. The enhanced near-surface H-down contribution in Supplementary Figure 4A and the representative O-down to H-down reorientation in Supplementary Figure 3 illustrate a geometry that favors H approach to Au(111). During O-H bond cleavage, hydrogen can approach the surface while the reacting oxygen relaxes toward the solution. This coupled motion is consistent with the greater reacting-oxygen distance and lower barrier from Li^+ to K^+ in Figure 4A and C. The proposed H-transfer-limited character on Au(111) describes this orientational contribution to hydrogen transfer during Volmer activation. Thus, the two branches of Figure 5D describe different local geometrical constraints on the same water-dissociation process.

The two proposed mechanisms explain how distinct interfacial geometries could yield the same association between a more outward reacting oxygen and a lower barrier within each metal series. On Pt(111), the analysis focuses on hydration of the developing hydroxide, whereas on Au(111) it focuses on the geometry of H approach. Both descriptions concern local cation-water coordination and solvent reorganization within the Volmer step[21,22,24]. The key result is that the calculated barriers reproduce the opposite experimental cation orderings qualitatively, even though the Raman and water-depletion responses change in the same direction on both metals. This agreement suggests that the Volmer barrier in the model may be an intrinsic contributing factor to the observed experimental trends. Recent Au(111) measurements also reveal an OH^--dependent enhancement of alkaline HER under independently varied electrolyte conditions[58]. Together, these findings place the possible intrinsic Volmer contribution within the broader dependence of HER kinetics on cation identity and hydroxide concentration.

CONCLUSIONS

Electrochemical measurements, Raman spectroscopy, and AIMD simulations reveal opposite cation effects on alkaline HER activity despite several similar changes in interfacial water on Pt and Au. Increasing cation size enhances the high-wavenumber Raman contribution and broadens the simulated water-depleted region on both metals. These trends alone do not predict the activity inversion. In contrast, the single-cation Volmer barrier increases from Li^+ to K^+ on Pt(111) and decreases on Au(111), reproducing the qualitative experimental ordering. Within each metal series, lower barriers correspond to greater reacting-oxygen distances, suggesting a role for metal-dependent coupling between cation position and reacting-water geometry. This agreement suggests that the model Volmer barrier may contribute intrinsically to the observed experimental trends.

DECLARATIONS

Authors' contributions

Performed the experiments and analyzed the data: Jin, F.; Cao, M.
Supervised the computational work and interpretation of the AIMD results: Tian, H.
Supervised the experimental work and coordinated the study: Zhu, C.

Provided overall conceptual guidance and supervision: Tong, S. Y.
Provided resources and technical support: Wang, X.; Zhang, W.; Shen, X.
All authors contributed to discussion of the results, revised the manuscript, and approved the final version.

Availability of data and materials

The data supporting the findings of this study are provided in the article and its Supplementary Materials. Further data are available from the corresponding authors upon request.

AI and AI-assisted tools statement

During the preparation of this manuscript, the GPT-5.6 (released 9 July 2026) was used only for language editing. The tool did not influence the research design, data collection, analysis, interpretation, or scientific content. All authors take responsibility for the accuracy, integrity, and final content of the manuscript.

Financial support and sponsorship

This work was financially supported by the National Natural Science Foundation of China (grant No. 12174326) and the Shenzhen Natural Science Foundation (grant No. GXWD20201231105722002-20200824163747001).

Conflicts of interest

Wang, X.; Zhang, W.; Shen, X. are affiliated with Inner Mongolia Huadian Huayang Hydrogen Energy Technology Co., Ltd. and Huadian Inner Mongolia Energy Co., Ltd. All other authors declare that they have no conflicts of interest.

Ethical approval and consent to participate

Not applicable.

Consent for publication

Not applicable.

Copyright

© The Author(s) 2026.

Supplementary Materials

Supplementary Materials

REFERENCES

1. Zhang, X.; Guo, Y.; Wang, C. Multi-interface engineering of nickel-based electrocatalysts for alkaline hydrogen evolution reaction. *Energy Mater* **2024**, *4*, 400044. DOI
2. Sheng, W.; Gasteiger, H. A.; Shao-Horn, Y. Hydrogen oxidation and evolution reaction kinetics on platinum: acid vs alkaline electrolytes. *J Electrochem Soc* **2010**, *157*, B1529. DOI
3. Zheng, J.; Sheng, W.; Zhuang, Z.; Xu, B.; Yan, Y. Universal dependence of hydrogen oxidation and evolution reaction activity of platinum-group metals on pH and hydrogen binding energy. *Sci Adv* **2016**, *2*, e1501602. DOI PubMed PMC
4. Nørskov, J. K.; Bligaard, T.; Logadottir, A.; et al. Trends in the exchange current for hydrogen evolution. *J Electrochem Soc* **2005**, *152*, J23. DOI
5. Ledezma-Yanez, I.; Wallace, W. D. Z.; Sebastián-Pascual, P.; Climent, V.; Feliu, J. M.; Koper, M. T. M. Interfacial water reorganization as a pH-dependent descriptor of the hydrogen evolution rate on platinum electrodes. *Nat Energy* **2017**, *2*, 17031. DOI
6. Mccrum, I. T.; Koper, M. T. M. The role of adsorbed hydroxide in hydrogen evolution reaction kinetics on modified platinum. *Nat Energy* **2020**, *5*, 891-9. DOI
7. Subbaraman, R.; Tripkovic, D.; Strmcnik, D.; et al. Enhancing hydrogen evolution activity in water splitting by tailoring Li^+-$Ni(OH)_2$-Pt interfaces. *Science* **2011**, *334*, 1256-60. DOI
8. Liu, E.; Li, J.; Jiao, L.; et al. Unifying the hydrogen evolution and oxidation reactions kinetics in base by identifying the catalytic roles of hydroxyl-water-cation adducts. *J Am Chem Soc* **2019**, *141*, 3232-9. DOI
9. Shah, A. H.; Zhang, Z.; Huang, Z.; et al. The role of alkali metal cations and platinum-surface hydroxyl in the alkaline hydrogen evolution reaction. *Nat Catal* **2022**, *5*, 923-33. DOI

10. Shah, A. H.; Zhang, Z.; Wan, C.; et al. Platinum surface water orientation dictates hydrogen evolution reaction kinetics in alkaline media. *J Am Chem Soc* **2024**, *146*, 9623-30. DOI
11. Rodellar, C. G.; Gisbert-Gonzalez, J. M.; Sarabia, F.; Roldan Cuenya, B.; Oener, S. Z. Ion solvation kinetics in bipolar membranes and at electrolyte-metal interfaces. *Nat Energy* **2024**, *9*, 548-58. DOI
12. Sarabia, F.; Gomez Rodellar, C.; Roldan Cuenya, B.; Oener, S. Z. Exploring dynamic solvation kinetics at electrocatalyst surfaces. *Nat Commun* **2024**, *15*, 8204. DOI PubMed PMC
13. Liang, W.; Cao, D.; Jia, Z.; et al. pH-dependent interaction of interfacial water with Pt in the electrocatalytic hydrogen oxidation reaction. *Nat Catal* **2026**, *9*, 998-1008. DOI
14. Chen, X.; Mccrum, I. T.; Schwarz, K. A.; Janik, M. J.; Koper, M. T. M. Co-adsorption of cations as the cause of the apparent pH dependence of hydrogen adsorption on a stepped platinum single-crystal electrode. *Angew Chem Int Ed* **2017**, *56*, 15025-9. DOI PubMed PMC
15. Jiao, L.; Liu, E.; Mukerjee, S.; Jia, Q. In situ identification of non-specific adsorption of alkali metal cations on Pt surfaces and their catalytic roles in alkaline solutions. *ACS Catal* **2020**, *10*, 11099-109. DOI
16. Garlyyev, B.; Xue, S.; Watzele, S.; Scieszka, D.; Bandarenka, A. S. Influence of the nature of the alkali metal cations on the electrical double-layer capacitance of model Pt(111) and Au(111) electrodes. *J Phys Chem Lett* **2018**, *9*, 1927-30. DOI
17. Xue, S.; Garlyyev, B.; Watzele, S.; et al. Influence of alkali metal cations on the hydrogen evolution reaction activity of Pt, Ir, Au, and Ag electrodes in alkaline electrolytes. *ChemElectroChem* **2018**, *5*, 2326-9. DOI
18. Monteiro, M. C. O.; Goyal, A.; Moerland, P.; Koper, M. T. M. Understanding cation trends for hydrogen evolution on platinum and gold electrodes in alkaline media. *ACS Catal* **2021**, *11*, 14328-35. DOI PubMed PMC
19. Goyal, A.; Louisia, S.; Moerland, P.; Koper, M. T. M. Cooperative effect of cations and catalyst structure in tuning alkaline hydrogen evolution on Pt electrodes. *J Am Chem Soc* **2024**, *146*, 7305-12. DOI PubMed PMC
20. Taji, Y.; Zagalskaya, A.; Evazzade, I.; et al. Alkali metal cations change the hydrogen evolution reaction mechanisms at Pt electrodes in alkaline media. *Nano Mater Sci* **2025**, *7*, 729-34. DOI
21. Zhu, X.; Binninger, T.; Koper, M. T. M.; Eikerling, M. Disentangling the Janus-faced effects of cations in electrocatalysis. *Nat Commun* **2026**, *17*, 3149. DOI PubMed PMC
22. Resasco, J. A universal model of cation effects in electrocatalysis. *JACS Au* **2025**, *5*, 5253-66. DOI PubMed PMC
23. De Kam, L. B.; Maier, T. L.; Krischer, K. Electrolyte effects on the alkaline hydrogen evolution reaction: a mean-field approach. *Electrochim Acta* **2024**, *497*, 144530. DOI
24. Bender, J. T.; Petersen, A. S.; Østergaard, F. C.; et al. Understanding cation effects on the hydrogen evolution reaction. *ACS Energy Lett* **2022**, *8*, 657-65. DOI
25. Li, P.; Jiang, Y.; Hu, Y.; et al. Hydrogen bond network connectivity in the electric double layer dominates the kinetic pH effect in hydrogen electrocatalysis on Pt. *Nat Catal* **2022**, *5*, 900-11. DOI
26. Tang, B.; Fang, Y.; Zhu, S.; et al. Tuning hydrogen bond network connectivity in the electric double layer with cations. *Chem Sci* **2024**, *15*, 7111-20. DOI PubMed PMC
27. Li, P.; Jiang, Y.; Men, Y.; Jiao, Y.; Chen, S. Kinetic cation effect in alkaline hydrogen electrocatalysis and double layer proton transfer. *Nat Commun* **2025**, *16*, 1844. DOI PubMed PMC
28. Xu, P.; Wang, R.; Zhang, H.; Carnevale, V.; Borguet, E.; Suntivich, J. Cation modifies interfacial water structures on platinum during alkaline hydrogen electrocatalysis. *J Am Chem Soc* **2024**, *146*, 2426-34. DOI
29. Kuroda, N.; Katase, A.; Hayashi, T.; Ikeda, K. Proton shuttling at electrochemical interfaces under alkaline hydrogen evolution. *Nat Commun* **2026**, *17*, 8328. DOI PubMed PMC
30. Chen, A.; Wang, Y.; Wang, X.; Yang, X.; Kuang, Y.; Le, J. Unifying the cation effects in alkaline hydrogen evolution reaction through atomistic simulations. *ACS Catal* **2025**, *16*, 1708-18. DOI
31. Le, J.; Chen, A.; Li, L.; et al. Modeling electrified Pt(111)-H_{ad}/water interfaces from *ab initio* molecular dynamics. *JACS Au* **2021**, *1*, 569-77. DOI
32. Tang, M. T.; Liu, X.; Ji, Y.; Norskov, J. K.; Chan, K. Modeling hydrogen evolution reaction kinetics through explicit water-metal interfaces. *J Phys Chem C* **2020**, *124*, 28083-92. DOI
33. Wilson, J. C.; Caratzoulas, S.; Vlachos, D. G.; Yan, Y. Insights into solvent and surface charge effects on Volmer step kinetics on Pt (111). *Nat Commun* **2023**, *14*, 2384. DOI PubMed PMC
34. Wang, Y.; Zheng, S.; Yang, W.; et al. In situ Raman spectroscopy reveals the structure and dissociation of interfacial water. *Nature* **2021**, *600*, 81-5. DOI
35. You, X.; Zhang, D.; Zhang, X.; et al. Exploring the cation regulation mechanism for interfacial water involved in the hydrogen evolution reaction by in situ Raman spectroscopy. *Nano-Micro Lett* **2023**, *16*, 53. DOI PubMed PMC

36. Kresse, G.; Furthmüller, J. Efficient iterative schemes for *ab initio* total-energy calculations using a plane-wave basis set. *Phys Rev B* **1996**, *54*, 11169-86. DOI
37. Kresse, G.; Joubert, D. From ultrasoft pseudopotentials to the projector augmented-wave method. *Phys Rev B* **1999**, *59*, 1758-75. DOI
38. Perdew, J. P.; Burke, K.; Ernzerhof, M. Generalized gradient approximation made simple. *Phys Rev Lett* **1996**, *77*, 3865-8. DOI PubMed
39. Grimme, S.; Antony, J.; Ehrlich, S.; Krieg, H. A consistent and accurate *ab initio* parametrization of density functional dispersion correction (DFT-D) for the 94 elements H-Pu. *J Chem Phys* **2010**, *132*, 154104. DOI PubMed
40. Methfessel, M.; Paxton, A. T. High-precision sampling for Brillouin-zone integration in metals. *Phys Rev B* **1989**, *40*, 3616-21. DOI
41. Marković, N. M.; Grgur, B. N.; Ross, P. N. Temperature-dependent hydrogen electrochemistry on platinum low-index single-crystal surfaces in acid solutions. *J Phys Chem B* **1997**, *101*, 5405-13. DOI
42. Ekspong, J.; Gracia-Espino, E.; Wågberg, T. Hydrogen evolution reaction activity of heterogeneous materials: a theoretical model. *J Phys Chem C* **2020**, *124*, 20911-21. DOI
43. Chun, J. H.; Ra, K. H.; Kim, N. Y. Langmuir adsorption isotherms of overpotentially deposited hydrogen at poly-Au and Rh/H_2SO_4 aqueous electrolyte interfaces: qualitative analysis using the phase-shift method. *J Electrochem Soc* **2003**, *150*, E207. DOI
44. Nosé, S. A unified formulation of the constant temperature molecular dynamics methods. *J Chem Phys* **1984**, *81*, 511-9. DOI
45. Hoover, W. G. Canonical dynamics: equilibrium phase-space distributions. *Phys Rev A* **1985**, *31*, 1695-7. DOI
46. Sprik, M.; Ciccotti, G. Free energy from constrained molecular dynamics. *J Chem Phys* **1998**, *109*, 7737-44. DOI
47. Singh-Miller, N. E.; Marzari, N. Surface energies, work functions, and surface relaxations of low-index metallic surfaces from first principles. *Phys Rev B* **2009**, *80*, 235407. DOI
48. Tran, R.; Xu, Z.; Radhakrishnan, B.; et al. Surface energies of elemental crystals. *Sci Data* **2016**, *3*, 160080. DOI PubMed PMC
49. Zhang, Q.; Sun, P.; Li, H.; Duan, Z. Synergistic cation-facet effects boost alkaline hydrogen evolution kinetics on stepped Pt surfaces. *Commun Chem* **2026**, *9*, 113. DOI PubMed PMC
50. Li, X. Y.; Wang, T.; Cai, Y. C.; et al. Mechanism of cations suppressing proton diffusion kinetics for electrocatalysis. *Angew Chem Int Ed* **2023**, *62*, e202218669. DOI
51. Li, C.; Chen, M.; Liu, S.; et al. Unconventional interfacial water structure of highly concentrated aqueous electrolytes at negative electrode polarizations. *Nat Commun* **2022**, *13*, 5330. DOI PubMed PMC
52. Groß, A.; Sakong, S. *Ab initio* simulations of water/metal interfaces. *Chem Rev* **2022**, *122*, 10746-76. DOI PubMed
53. Momma, K.; Izumi, F. *VESTA 3* for three-dimensional visualization of crystal, volumetric and morphology data. *J Appl Crystallogr* **2011**, *44*, 1272-6. DOI
54. Xue, S.; He, X.; Tu, Z.; et al. An efficient and durable low-iridium catalyst enabled by a potential-triggered dual-pathway mechanism for acidic water oxidation. *Adv Mater* **2026**, *38*, e74113. DOI PubMed PMC
55. Waegele, M. M.; Gunathunge, C. M.; Li, J.; Li, X. How cations affect the electric double layer and the rates and selectivity of electrocatalytic processes. *J Chem Phys* **2019**, *151*, 160902. DOI
56. Mähler, J.; Persson, I. A study of the hydration of the alkali metal ions in aqueous solution. *Inorg Chem* **2011**, *51*, 425-38. DOI PubMed PMC
57. Hagopian, A.; Louisia, S.; Boterman, K.; Doblhoff-Dier, K.; Koper, M. Molecular insights into the double-layer capacitance of platinum surfaces in alkaline media. *JACS Au* **2026**, *6*, 2345-54. DOI PubMed PMC
58. Zhen, E.; Zong, T.; Zhu, B.; et al. OH^--enhanced alkaline hydrogen evolution reaction at the Au(111) electrode. *J Catal* **2026**, *453*, 116525. DOI

Disclaimer/Publisher's Note: All statements, opinions, and data contained in this publication are solely those of the individual author(s) and contributor(s) and do not necessarily reflect those of OAE and/or the editor(s). OAE and/or the editor(s) disclaim any responsibility for harm to persons or property resulting from the use of any ideas, methods, instructions, or products mentioned in the content.

© The Author(s) 2026. Open Access This article is licensed under a Creative Commons Attribution 4.0 International License (https://creativecommons.org/licenses/by/4.0/), which permits unrestricted use, sharing, adaptation, distribution and reproduction in any medium or format, for any purpose, even commercially, as long as you give appropriate credit to the original author(s) and the source, provide a link to the Creative Commons license, and indicate if changes were made.